

## Article

# Demagnetization Modeling and Analysis for a Six-Phase Surface-Mounted Field-Modulated Permanent-Magnet Machine Based on Equivalent Magnetic Network

Xianglin Li, Yingjie Tan, Bo Yan <sup>\*</sup>, Yujian Zhao and Hao Wang

College of Electrical Engineering, Qingdao University, Qingdao 266071, China; lxllcc@126.com (X.L.); tanyingjie95@126.com (Y.T.); 2021020635@qdu.edu.cn (Y.Z.); wanghao0573@126.com (H.W.)

\* Correspondence: yb\_qdu@qdu.edu.cn

**Abstract:** Based on the magnetic gear effect, the field-modulated permanent-magnet machine (FMPMM) can realize the unequal pole design of the rotor PM field and the stator armature magnetic field. With the advantages of high torque density and high efficiency, the FMPMM has been widely studied in low-speed direct-drive applications. As a kind of machine excited by PMs, the performance of the FMPMM was affected by the demagnetization state. However, the method for establishing the FMPMM demagnetization model based on a finite element analysis (FEA) presented some problems, including tedious repeated modeling work and long calculation time-consuming under fine subdivision. Therefore, in this paper, a six-phase surface-mounted FMPMM was taken as an example, and an equivalent magnetic network (EMN) model was proposed for evaluating the machine performance under demagnetization. In order to realize the rapid establishing EMN models under diverse demagnetization types, the variable coercivity of PM was introduced. Furthermore, for the purpose of improving the calculation accuracy and shortening the calculation time, the least square method was used in fitting and analyzing the discrete results. Then, in order to verify the validity of the proposed EMN model, a prototype was fabricated and a testing platform was built. The air-gap flux density and the no-load back EMF obtained by the FEA, the proposed EMN model, and the experimental testing were compared. The results showed that the proposed EMN model can realize the rapid modeling and accurate analysis of the six-phase surface-mounted FMPMM under diverse demagnetization types.

**Keywords:** demagnetization modeling; equivalent magnetic network (EMN); field-modulated permanent-magnet machine (FMPMM)



**Citation:** Li, X.; Tan, Y.; Yan, B.; Zhao, Y.; Wang, H. Demagnetization Modeling and Analysis for a Six-Phase Surface-Mounted Field-Modulated Permanent-Magnet Machine Based on Equivalent Magnetic Network. *Energies* **2023**, *16*, 6099. <https://doi.org/10.3390/en16166099>

Academic Editor: Anibal De Almeida

Received: 20 July 2023

Revised: 8 August 2023

Accepted: 15 August 2023

Published: 21 August 2023



**Copyright:** © 2023 by the authors. Licensee MDPI, Basel, Switzerland. This article is an open access article distributed under the terms and conditions of the Creative Commons Attribution (CC BY) license (<https://creativecommons.org/licenses/by/4.0/>).

## 1. Introduction

In recent years, as a new type of machine, the field-modulated permanent-magnet machine (FMPMM) has received much attention [1,2]. Equipped with the advantages of high torque density, high efficiency, and low torque ripple due to magnetic gearing effect [3], the FMPMM has been studied extensively in the fields of low-speed direct-drive applications such as wind power generation [4], tidal power generation [5], electric vehicle [6], and ship propulsion [7,8]. However, the FMPMM is still excited by permanent magnet (PM), which is prone to local or uniform demagnetization due to working temperature [9], armature reaction [10], manufacturing defects, and service life [11]. Then, the FMPMM will face performance degradation including an output torque decrease and a torque ripple increase [12]. These faults will in turn increase the risk of serious demagnetization or even damage to machine performance [13–16]. Therefore, in order to ensure the stability of FMPMM, it is necessary to diagnose and analyze its demagnetization state. For FMPMM diagnose system, the electromagnetic characteristic data under demagnetization are essential. In common, the electromagnetic data under demagnetization can be obtained with the help of the machine demagnetization model. However, the existing methods used for establishing

the FMPMM demagnetization model are insufficient in accuracy under shorter calculation time [17–19].

Based on the research status, the methods for establishing the FMPMM model can be divided into three categories: the analytical model method [20–22], the finite element analysis (FEA) [17–19,23,24] and the equivalent magnetic network (EMN) [25,26]. In [27], an analytical model of the FMPMM was established by the subdomain method. Although this method is based on the principle of precise angle mapping, which can accurately reflect the relationship between slotted air-gap and slot-less air-gap of the FMPMM and accurately obtain the magnetic field distribution, there are some problems including complex modeling process, slow calculation speed. In [23], a split-tooth concentrated-winding FMPMM using ferrite magnets with low coercivity was analyzed by the FEA, and the influence of PM shape and size on the machine under demagnetization was emphatically studied. Although the FEA has a high accuracy, there are some problems including complicated modeling process and long calculation time under large number of grids. In [28], an EMN model combining the adaptive grid method has been proposed to efficiently analyze the characteristics of a vehicular dual-PM FMPMM.

At present, although the EMN method has been used in establishing the FMPMM model, there is little discussion on modeling the FMPMM demagnetization model based on the EMN. Therefore, a method for establishing a six-phase surface-mounted FMPMM demagnetization model based on the EMN is presented in this paper. By introducing the variable coercivity and appropriate curve-fitting method, the proposed EMN model can realize the rapid and accurate modeling. Compared with the FEA, the proposed EMN model has a faster calculation speed. Furthermore, based on the proposed EMN model, the no-load back electromotive force (EMF) and air-gap flux density under demagnetization can be calculated flexibly. Then, in order to verify the accuracy of the proposed EMN model, a prototype was fabricated. The no-load back EMF waveforms and air-gap flux density waveforms obtained by the proposed EMN model, the FEA, and the experimental testing were comparatively analyzed. The comparison results show that the proposed EMN model is in good agreement with the FEA and experiments.

## 2. EMN Modeling of Six-Phase Surface-Mounted FMPMM under Demagnetization

### 2.1. Machine Topology

In this paper, the studied six-phase surface-mounted FMPMM adopts the conventional topology type of outer stator and inner rotor. As shown in Figure 1, the machine topology is relatively compact with a single-layer centralized armature winding. The stator teeth are parallel without the pole shoe, the stator slot is slotted, and the PM is surface mounted. Two windings in the same phase (e.g., A1 and A2) are connected in series. The six-phase currents of the stator are shown in Figure 2. In addition, the main parameters of the analyzed machine are shown in Table 1.

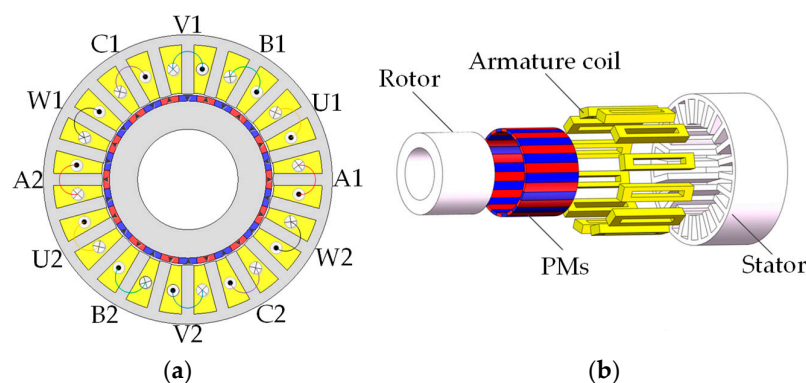


**Figure 1.** Topology of the six-phase surface-mounted FMPMM, (a) 2-D view, (b) 3-D view.

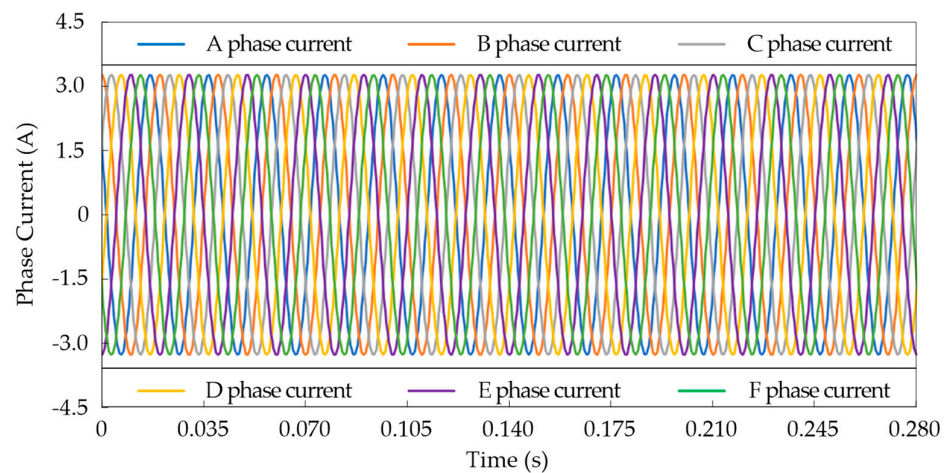


**Figure 2.** The six-phase currents of the stator.

**Table 1.** The main parameters of the analyzed six-phase surface-mounted FMPMM.

Parameters	Value	Unit
Rated speed	214	r/min
Rated power	250	W
Phase voltage	18	V
Phase current	2.3	A
PM pole number of rotor	28	-
Number of stator tooth	24	-
Pole-pair number of armature winding	10	-
Number of turns per armature coil	119	-
Stack length	60	mm
Air-gap length	1.5	mm
Material of iron core	35CS250	-
Material of PMs	N38SH	-
Thickness of PM	4	mm
Inner radius of rotor	25	mm
Outer radius of rotor	42	mm
Inner radius of stator	43.5	mm
Outer radius of stator	72	mm
Thickness of stator yoke	5	mm
Width of stator tooth	4	mm

## 2.2. Magnetic Field Distribution

In this paper, the FEA model of the six-phase surface-mounted FMPMM was established, and the simulation in different demagnetization degrees was realized by changing the coercive force  $H_C$  of permanent magnets. The degree of uniform demagnetization of single PM is  $T$ , which is determined as follows:

$$T = 1 - \frac{H_C}{H_{C0}} \quad (1)$$

where  $H_{C0}$  is the coercivity of PM without demagnetization.

In order to establish an accurate EMN model, the magnetic circuit should be divided reasonably according to the magnetic field distribution. The irreversible uniform demagnetization of the single permanent magnet is simulated by the FEA. As shown in Figure 3, the magnetic flux density inside the demagnetized PM is obviously reduced but remains uniform. The reduction proportion of the magnetic flux density increases when the PM demagnetization worsens. However, in the demagnetized PM, the magnetic flux density between the air-gap and the stator teeth not only decreases, but also becomes extremely uneven, especially near the stator teeth tip, which makes it difficult to accurately calculate

the air-gap permeance between the stator and the rotor. Therefore, in this paper, the subsection method is introduced to analyze the stator teeth under PM demagnetization, and the calculation method of the air-gap permeance in the demagnetized PM is improved.

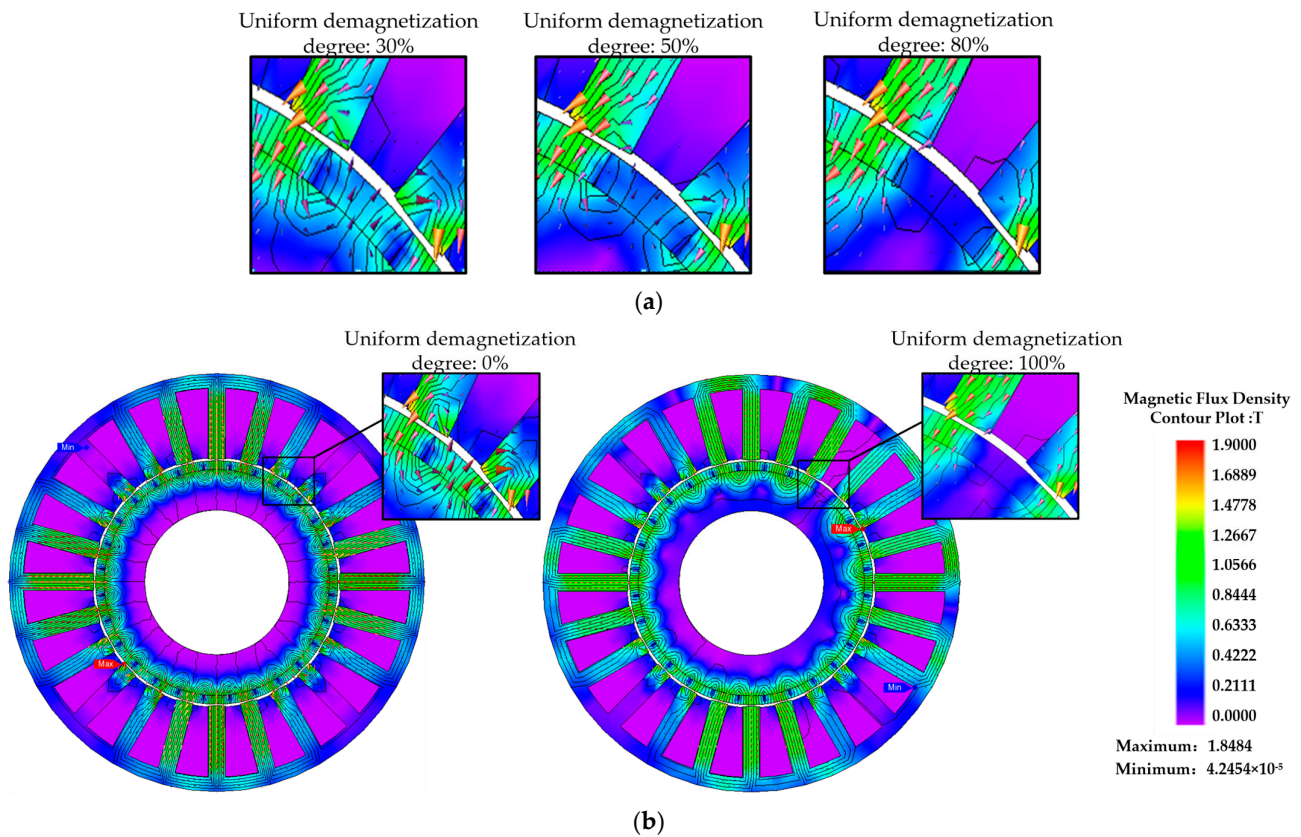


**Figure 3.** Magnetic field distributions of six-phase surface-mounted FPM under different demagnetization degrees, (a) partial view, (b) entire view.

### 2.3. Stator EMN Model

The principle of modeling based on EMN is dividing the magnetic circuit of the machine into a certain number of grids. Then, based on the shape, the permeance of these grids can be obtained. As shown in Figure 4, the stator of six-phase surface-mounted FPM includes three parts: the stator yoke, the stator tooth, and the stator slot.

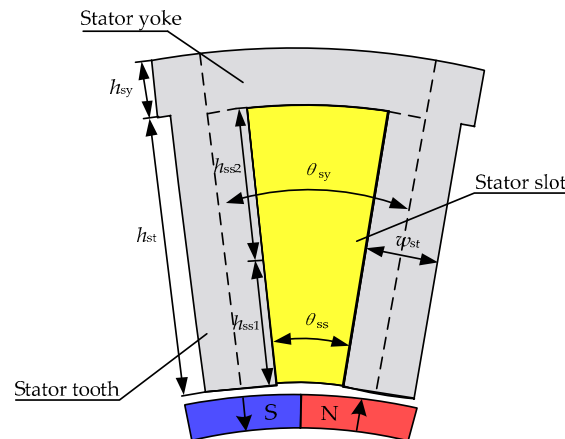


**Figure 4.** The main parameters of the stator.

Firstly, the entire stator of the six-phase surface-mounted FMPMM is evenly divided into 24 parts, and each part includes one stator tooth, one stator yoke and one stator slot. From the above analysis, the magnetic flux density is uniform in the stator yoke and uneven in the stator tooth. At the same time, due to the obvious edge effect, the leakage flux of the stator slot is larger at the teeth tip and smaller at the teeth root. Therefore, in order to establish an accurate EMN demagnetization model, the stator yoke is divided into one grid. The stator tooth is divided into two grids: one stator tooth tip grid and one stator tooth root grid. Meanwhile, the stator slot near the stator tooth tip is divided into one grid, and the part near the stator tooth root is ignored. In the magnetic circuit, the armature winding does not directly conduct magnetic flux, but generates the MMF in the magnetic circuit through the armature reaction. Therefore, the armature winding is only equivalent to the stator MMF source  $F_a$ . The magnitude of the stator MMF source is determined by the armature current, which can be ignored when the machine is unloaded. Then, the permeance of each grid is calculated according to its shape, which is shown in Table 2, where  $\mu_{sy}$  is the permeability of stator yoke,  $l_s$  is the machine shaft length,  $\theta_{sy}$  is the angle of the stator yoke,  $h_{st}$  is the height of the stator tooth,  $R_{rt}$  is the inner radius of the stator,  $\mu_{st}$  is the permeability of the stator tooth,  $w_{st}$  is the width of the stator tooth,  $h_{ss1}$  and  $h_{ss2}$  is the height of the stator slot, and  $\theta_{ss}$  is the angle of the stator slot,  $I_n$  is current in the  $n$ -th stator slot, and these parameters are shown in Figure 4. Finally, linking all the grid permeance according to the magnetic circuit, the six-phase surface-mounted FMPMM stator model based on EMN can be established as shown in Figure 5. In addition, the iron core permeability makes changes in term of the saturation of the ferromagnetic material. Therefore, it is necessary to update the iron core permeability in each iteration. In this paper, the look-up table method introduced in the third chapter was used to update the iron core permeability.

Table 2. The permeance calculation for stator grids.

Terms	Symbol	Equations
Permeance of stator yoke-1	$G_{sy1}$	$G_{sy1} = \mu_{sy} l_s \ln((h_{sy} + 2h_{st} + R_{st})/w_{sy})/\theta_{sy}$
Permeance of stator yoke-2	$G_{sy2}$	$G_{sy2} = \mu_{sy} l_s \theta_{sy} / \ln((h_{sy} + 2h_{st} + R_{st})/w_{sy})$
Permeance of stator tooth-1	$G_{st1}$	$G_{st1} = 1.538 \mu_{st} l_s w_{st} / h_{st}$
Permeance of stator tooth-2	$G_{st2}$	$G_{st2} = 2.857 \mu_{st} l_s w_{st} / h_{st}$
Permeance of Leakage flux-1	$G_{\delta 1}$	$G_{\delta 1} = \mu_0 l_s \ln((h_{ss1} + h_{ss2} + R_{st})/h_{ss2})/\theta_{ss}$
Permeance of Leakage flux-2	$G_{\delta 2}$	$G_{\delta 2} = 2\mu_0 l_s \theta_{ss} / \ln((h_{ss1} + h_{ss2} + R_{st})/(h_{ss1} + h_{ss2}))$
Permeance of Leakage flux-3	$G_{\delta 3}$	$G_{\delta 3} = \mu_0 l_s \ln((h_{ss1} + R_{st})/h_{ss1})/\theta_{ss}$
MMF source of stator tooth	$F_a$	$F_a = \sum_{n=1}^{23} (n - 24) I_n / 24 + \sum_{n=1}^a I_n$

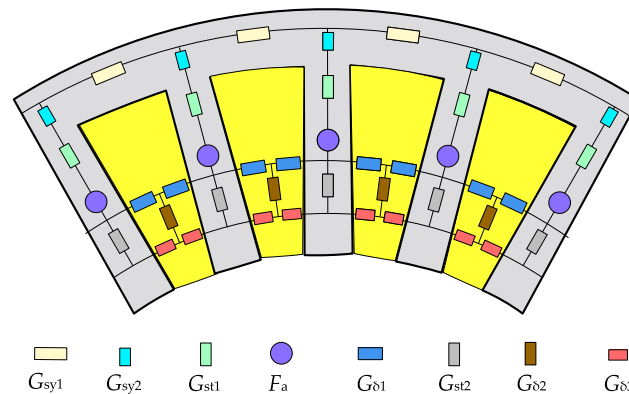


Figure 5. The EMN model of the stator.

### 2.4. Rotor EMN Model

Unlike conventional permanent magnet synchronous motors, in which only one working harmonic contributed to the torque transmission, multi-harmonics are used in

field modulation motors to achieve a high torque density [29]. Therefore, in order to improve the accuracy of the model, the PM and rotor iron core are divided into multiple grids. However, the multiple grids also extend the calculation time of the model. Therefore, in order to shorten the calculation time of the proposed EMN model under acceptable accuracy, the number of the PM grids along the tangential direction should be determined reasonably in the modeling. Firstly, the entire rotor iron core of the six-phase surface-mounted FMPMM is evenly divided into 28 parts. In this paper, 1–6 are used as the grid number of one PM and one rotor iron core part along the tangential direction. The six EMN models are established in turn, and the air-gap flux density and calculation time are compared with the FEA, respectively. The comparison results are shown in Table 3, where the error is the percentage error between the FEA and the EMN model. It is easy to see that the percentage error of the established EMN model is small and the calculation time is short when one PM and one rotor iron core part is divided in four grids along the tangential direction. And then, the rotor iron core is divided again along the radial direction. From the analysis above, it is known that under the demagnetization the rotor iron core magnetic field is stronger in the part close to the PM and weaker in the part close to the machine shaft. Therefore, in this paper, the rotor iron core part was divided into two areas along the radial direction: the effective area and the invalid area. With one-half of the rotor iron core radius as the boundary, the area between the boundary and the rotor iron core outer surface is the effective area, and the other part of rotor iron core is the invalid area. Finally, the rotor is divided as shown in Figure 6. Taking 1# PM as an example, it is divided into adjacent four grids along the tangential direction, denoted as PM1-1, PM1-2, PM1-3, and PM1-4, and the correspondence rotor iron core is also divided into four grids in effective area, denoted as RS1-1, RS1-2, RS1-3, and RS1-4.

**Table 3.** Comparison of the air-gap flux density and the calculation time of six EMN models.

Divided Grids	Error	Calculation Time
1	23.24%	10.26 s
2	16.28%	44.33 s
3	10.30%	74.04 s
4	3.02%	102.02 s
5	2.33%	282.45 s
6	2.14%	686.92 s

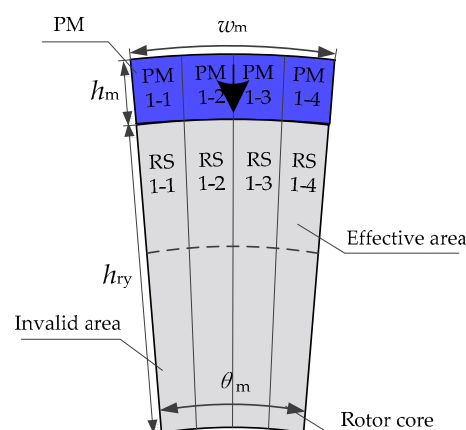


**Figure 6.** The main parameters of the rotor.

Finally, as listed in Table 4, the permeance can be calculated according to the grid shape, where  $w_m$  is the width of PM,  $H_C$  is the coercivity of PM,  $H_{C0}$  is the initial coercivity of PM without demagnetization,  $h_m$  is the radial thickness of PM,  $T$  is defined as the demagnetization degree of PM ( $0 \leq T \leq 1$ , and  $T = 1$  means the demagnetization degree 100%),  $\theta_m$  is the angle of PM,  $h_{ry}$  is the radial thickness of the rotor iron core,  $R_{ry}$  is the

inner radius of the rotor,  $\mu_{ry}$  is the permeability of the rotor iron core, and these parameters are shown in Figure 6. Also, in the iterative calculation, the iron core permeability also needs to be updated by the look-up table method.

**Table 4.** The permeance calculation for rotor grids.

Terms	Symbol	Equations
Permeance of rotor yoke-1	$G_h$	$G_h = 4\mu_{ry}l_s \ln((h_{ry} + R_{ry})/0.5h_{ry})/\theta_m$
Permeance of rotor yoke-2	$G_i$	$G_i = 0.25\mu_{ry}l_s\theta_m/\ln((h_{ry} + R_{ry})/h_{ry})$
Permeance of rotor yoke-3	$G_j$	$G_j = 4\mu_{ry}l_s \ln((0.5h_{ry} + R_{ry})/0.5h_{ry})/\theta_m$
Permeance of PM	$G_m$	$G_m = 0.25\mu_0l_s w_m/h_m$
MMF source of PM	$F_m$	$F_m = H_C h_m = (1 - T)H_0 h_m$

In order to reduce the calculation time of the proposed EMN model, the PM node of the rotor EMN model can be simplified, and the MMF calculation of the PM under the demagnetization can be improved. The method is introduced as follows: in case the difference of  $T$  between the two adjacent PMs is relatively large, the two PM parallel branches can be simplified to an equivalent PM branch. The PM branch with a smaller  $T$  is replaced by the equivalent PM branch, and the PM branch with a larger  $T$  is removed. Namely, the coercivity of the PM with a larger  $T$  is set as 0, and the corrected coercivity of the equivalent PM branch is defined as

$$H'_{Ci} = \begin{cases} \frac{(T_{i+1}-T_i)H_{C0}G_i}{G_i+G_{i+1}} + (1-T_{i+1})H_{C0} & (|T_i - T_{i+1}| > D_{THR}) \\ (1-T_i)H_{C0} & (|T_i - T_{i+1}| \leq D_{THR}) \end{cases} \quad (2)$$

where  $H'_{Ci}$  is the corrected coercivity of the equivalent  $i$ -th PM,  $T_i$  is the demagnetization degree of the  $i$ -th PM,  $G_i$  is the air-gap permeance connected to the  $i$ -th PM,  $D_{THR}$  is the threshold of the difference of  $T$  between the two adjacent PMs.

In order to determine the most suitable  $D_{THR}$ , the no-load back EMF error and the calculation time of the proposed EMN model under different thresholds are compared, and the results are shown in Table 5. It can be seen that the no-load back EMF error is acceptable at  $D_{THR} \geq 0.70$ , and the calculation time is reduced accordingly with the decrease in the threshold value. In this paper, considering these two aspects, the  $D_{THR}$  is selected as 0.70.

**Table 5.** Comparison of the no-load back EMF and the calculation time of six EMN models employing different thresholds.

Thresholds	Error	Calculation Time
0.25	9.87%	212.56 s
0.40	6.97%	238.48 s
0.55	3.26%	262.24 s
0.70	0.43%	282.45 s
0.85	0.14%	302.45 s
1.00	0%	322.65 s

In addition, as the rotor EMN model, the rotor iron core permeability needs to be updated at each iteration step of the calculation. As shown in Figure 7, connecting all the rotor permeance according to the magnetic circuit, the six-phase surface-mounted FMPMM rotor EMN model can be finally established.

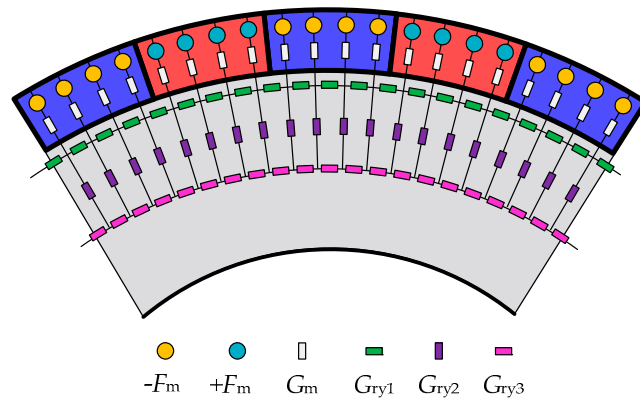


Figure 7. The EMN model of the rotor.

2.5. Air-Gap EMN Model

In this paper, in terms of the six-phase surface-mounted FMPMM, the established EMN model contains 24 stator teeth tip grids and 112 PM grids. One stator tooth tip grid and one PM grid are both linked by an air-gap grid. The permeance of the air-gap grid can be determined by the relative position of the stator and the rotor. For each position of the rotor, the air-gap permeance can be calculated by the fitting curve summarized by Ostovic [30–34]. As shown in Figure 8, the specific calculation process is as follows: the angle between the stator tooth and the PM is  $x$ , and the equation between the air-gap permeance and  $x$  can be expressed as shown in Table 6, where  $g$  is the air-gap length, and  $x_t$  and  $x'_t$  can be expressed as

$$x_t = \frac{2w_{st1} + 0.5w_m}{R_{st} + R_{sy} + 0.5h_{ry} + h_m} \tag{3}$$

$$x'_t = \frac{2w_{st1} - 0.5w_m}{R_{st} + R_{sy} + 0.5h_{ry} + h_m} \tag{4}$$

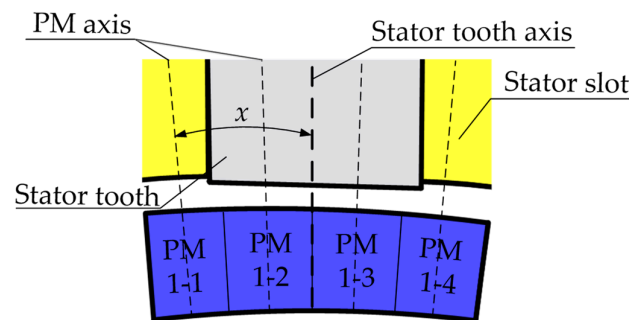


Figure 8. Drawing of relative position of stator and rotor.

Table 6. The equations for air-gap permeance calculation.

Value Interval of $x$	Equations
$[0, x'_t]$	$0.25\mu_0 l_s w_m / g$
$[x'_t, x_t]$	$0.125\mu_0 l_s w_m (1 + \cos(\pi(x - x'_t) / (x_t - x'_t))) / g$
$[x_t, 2\pi - x_t]$	$0.125\mu_0 l_s w_m (1 + \cos(\pi(x - x'_t - 2\pi) / (x_t - x'_t))) / g$
$[2\pi - x_t, 2\pi - x'_t]$	0
$[2\pi - x'_t, 2\pi]$	$0.25\mu_0 l_s w_m / g$

After that, the complete EMN demagnetization model of the six-phase surface-mounted FMPMM can be obtained by connecting the stator, rotor and air-gap EMN models established above.

### 3. Calculation Process of the Proposed EMN Model

#### 3.1. Iterative Calculation

In this paper, the proposed EMN model is composed of circuit branches and nodes, and each permeance belongs to an independent circuit branch. The MMF source is contained in these independent circuit branches, and the intersection of any two independent circuit branches is a node. According to the connection of circuit branches, the following matrix is defined. The incidence matrix of the proposed EMN model is  $A$ , reflecting the connection of these circuit branches. The circuit branch permeance matrix is  $G$ , composed of all permeances. The node magnetomotive force (MMF) matrix is  $F_n$ , and the circuit branch MMF source matrix is  $F_s$ . The elements in  $F_n$  are the MMF of all nodes compared to the reference node, which are unknown quantities. The element in  $F_s$  is the MMF source obtained by PM, which is a known quantity, namely  $F_m$  in Table 4. The node MMF equation of the proposed EMN model is established by imitating the circuit node voltage equation, which is expressed as follows

$$f(F_n) = AG(A^T F_n + F_s) = 0 \quad (5)$$

where  $A^T$  is the transposition of  $A$ .

From the above analysis,  $G$  is a nonlinear matrix. Therefore, in order to solve the nonlinear equation and improve the iteration speed, the Newton–Raphson method is introduced. The iterative equation is as follows

$$F_n^{k+1} = F_n^k - J^{-1}(F_n^k)f(F_n^k) \quad (6)$$

where  $J^{-1}(F_n)$  is the Jacobian matrix of the function  $f(F_n)$ .

In the iterative process, the iron core permeability makes changes in terms of the saturation of the ferromagnetic material. Therefore, in order to obtain the accurate circuit branch permeance matrix, the circuit branch magnetic field strength matrix should be updated in real time. The equation of the circuit branch magnetic field strength matrix is given as

$$H^k = (A^T F_n^k + F_s)L^{-1} \quad (7)$$

where  $L$  is the effective magnetic path length matrix composed of the magnetic path length along the magnetic flux conduction direction in all independent branches, and  $L^{-1}$  is the inverse matrix of  $L$ .

Figure 9 shows the specific steps of the iterative calculation process, in which the maximum error  $e$  is set as  $10^{-5}$ .

In this paper, the look-up table method is used to update the iron core permeability. According to the B-H curve (35C250 iron core material), the magnetic flux density is determined by the magnetic field strength of iron core grid calculated by Equation (7), and the ratios between them are the permeability of each iron core grid.

#### 3.2. Air-Gap Flux Density and Back-EMF Calculation

The solution of iterative calculation is the node MMF matrix  $F_n$ , and the magnetic flux density  $B$  can be calculated as follows

$$B = \frac{AGA^T F_n L^{-1}}{l_s} \quad (8)$$

Thus, the phase back EMF can be calculated as

$$E_p = -\frac{\partial \Psi}{\partial t} \quad (9)$$

where  $\psi$  is the phase flux linkage, which can be expressed as

$$\Psi = N(\Delta F_1 G_1 + \Delta F_2 G_2) \quad (10)$$

where  $N$  is the number of turns per phase winding,  $\Delta F_1$  and  $\Delta F_2$  are the MMF of the stator tooth belonging to the one phase winding, respectively, and  $G_1$  and  $G_2$  are the permeance of the stator tooth belonging to the one phase winding, respectively.

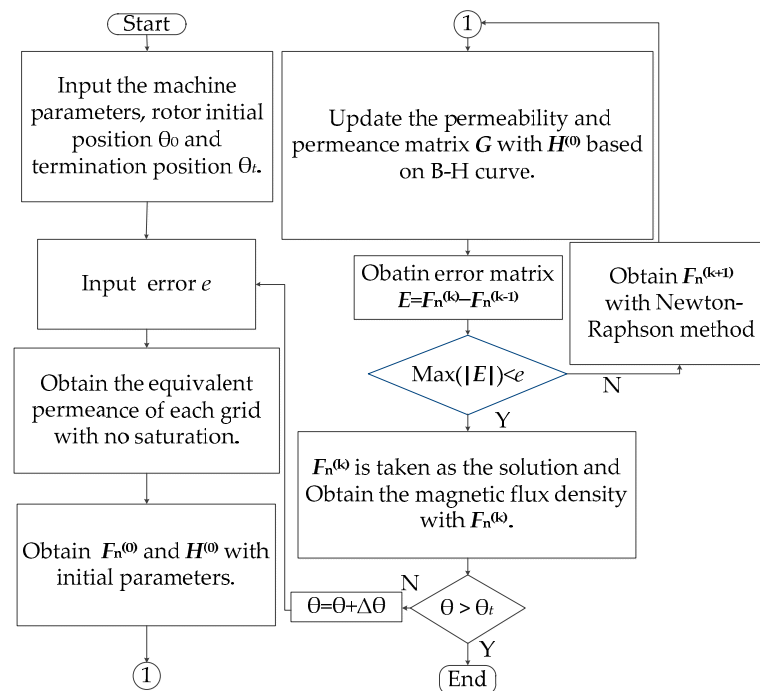


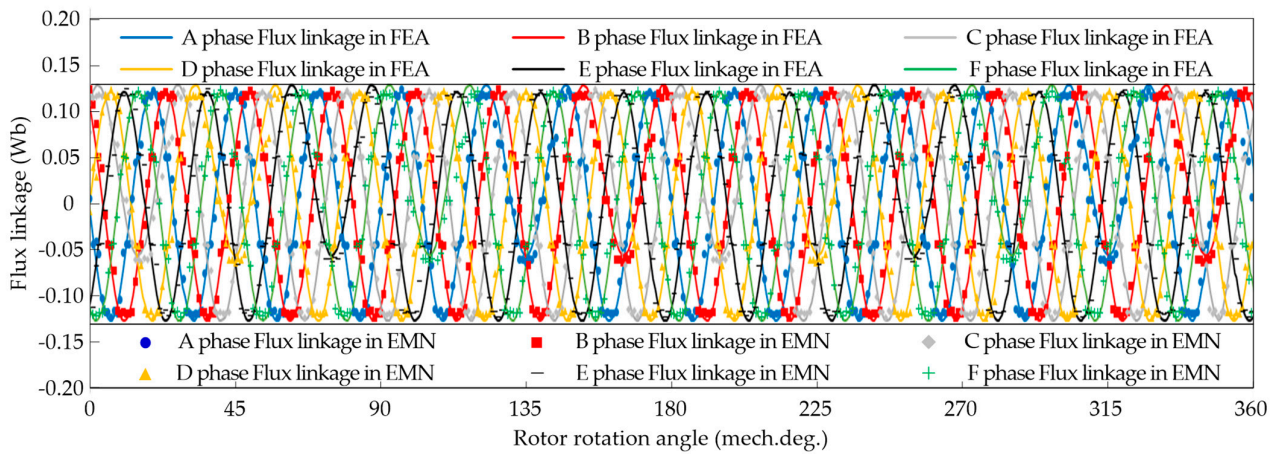
**Figure 9.** The flow chart of iterative calculation process.

### 3.3. Curve-Fitting Method

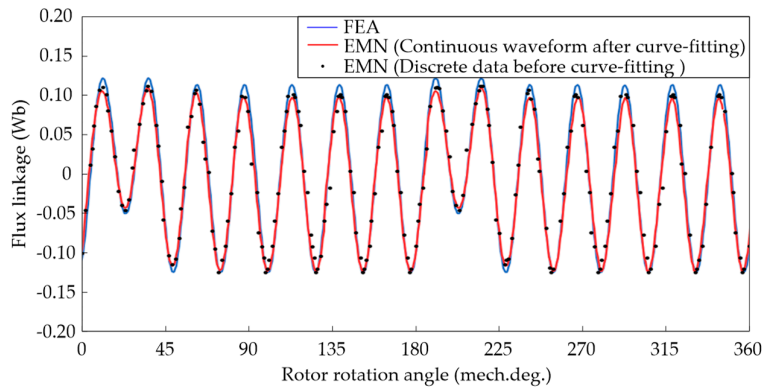
From the above iterative calculation, the back EMF (discrete data) of each grid can be obtained. The back-EMF waveform is more continuous by dividing more grids in establishing the six-phase surface-mounted FMPMM demagnetization model based on the EMN. However, the calculation time of the proposed EMN model is extended with more grids. Therefore, in order to reduce the calculation time and ensure the accuracy of the proposed EMN model, the curve-fitting method is introduced. In numerical analysis, the curve-fitting method is an effective method for fitting discrete data. Under the appropriate criteria, a function closest to all data points is obtained with the least-square-based fitting method. Table 7 shows a series of common curve-fitting functions. Eventually, in order to obtain the completely continuous back EMF waveform, the flux linkage (discrete data) should be fitted first. As shown in Figure 10, the phase flux-linkage waveform of the six-phase surface-mounted FMPMM based on FEA is approximately sinusoidal. Therefore, the Fourier function is introduced for its optimal fit. It can be seen from Figure 10 that the phase flux-linkage waveform after the curve-fitting from the proposed EMN model becomes continuous and well matches the waveform obtained by the FEA.

**Table 7.** The common curve-fitting methods.

Methods	Equations
Exponential	$aexp(bx)$ or $\{aexp(bx) + cexp(dx)\}$
Fourier	$a_0 + a_1\cos(wx) + b_1\sin(wx)$
Gaussian	$a_1\exp\left(-((x - b_1)/c_1)^2\right)$
Power	$ax^b$ or $\{ax^b + c\}$
Rational	$a/(x + b)$
Sum of Sin Functions	$a_1\sin(b_1x + c_1)$
Weibull	$abx^{b-1}\exp(-ax^b)$



(a)



(b)

**Figure 10.** The comparison of phase flux-linkage waveforms, (a) six-phase flux linkage, (b) single phase flux linkage.

#### 4. Comparison Analysis with the FEA

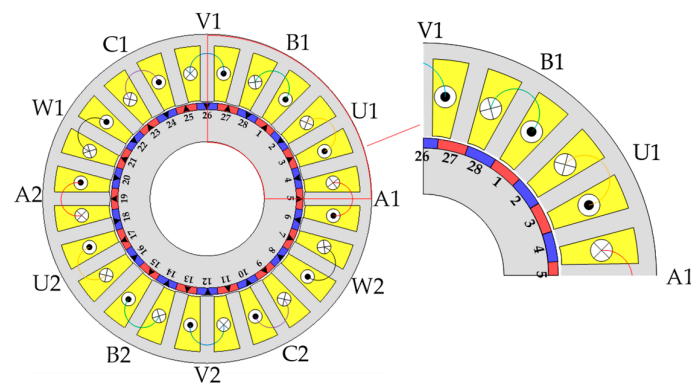
##### 4.1. Parameter Setting

In order to verify the accuracy of the six-phase surface-mounted FMPMM demagnetization model based on the proposed EMN method, eight common demagnetization types are presented in this paper. In addition, for these common demagnetization types, the no-load back-EMF waveform and the air-gap flux density waveform obtained by the proposed EMN model and FEA are compared at the rated speed. These eight common PM demagnetization types are summarized in Table 8. The demagnetization in Table 8 is irreversible. Under the normal operation of the machine, the degree of irreversible demagnetization is not affected by the stator phase current.

**Table 8.** The analyzed demagnetization types in this paper.

Groups	Types	Demagnetization Degree		
		PM1	PM2	PM3
Group 1	Type 1-1	100%	0%	0%
	Type 1-2	100%	100%	0%
	Type 1-3	100%	0%	100%
	Type 1-4	100%	100%	100%
Group 2	Type 2-1	35%	0%	0%
	Type 2-2	50%	0%	0%
	Type 2-3	65%	0%	0%
	Type 2-4	80%	0%	0%

Note: The demagnetization degree of other PMs is 0%, and the PM number is defined in Figure 11.

**Figure 11.** PM number definition.

#### 4.2. Result Comparison Analysis

In order to more intuitively reflect the discrepancy of the no-load back EMF waveforms obtained by the proposed EMN model and the FEA, the transient error of the no-load back EMF between the EMN and FEA is  $\delta_1$ , which is defined as

$$\delta_1(t) = \frac{v_{EMN}(t) - v_{FEA}(t)}{V_{peak}} \times 100\% \quad (11)$$

where  $v_{EMN}(t)$  is the no-load back EMF obtained by the proposed EMN model at time  $t$ ;  $v_{FEA}(t)$  is the no-load back EMF obtained by the FEA at time  $t$ ;  $V_{peak}$  is the peak value of the no-load back EMF obtained by the proposed EMN model.

That is, the transient error  $\delta_1$  represents the instantaneous error between the back EMF waveforms obtained by the proposed EMN model and the FEA. In addition, in order to discuss the steady error between them, the Mean Absolute Error (MAE) of the transient error  $\delta_1$  is defined as follows

$$M_1 = \frac{\int_{t_1}^{t_2} |\delta_1(t)| dt}{t_2 - t_1} \quad (12)$$

For demagnetization Group 1, the result comparison between the FEA and the proposed EMN model in the condition of the constant rated rotating speed of the rotor is shown in Figure 12. The air-gap flux density waveform obtained by the proposed EMN model almost matches the FEA results. And it can be seen the absolute value of the transient error  $\delta_1$  is less than 8.1%, and  $M_1$  is between 1.99% and 2.49%, which means that there is a good agreement.

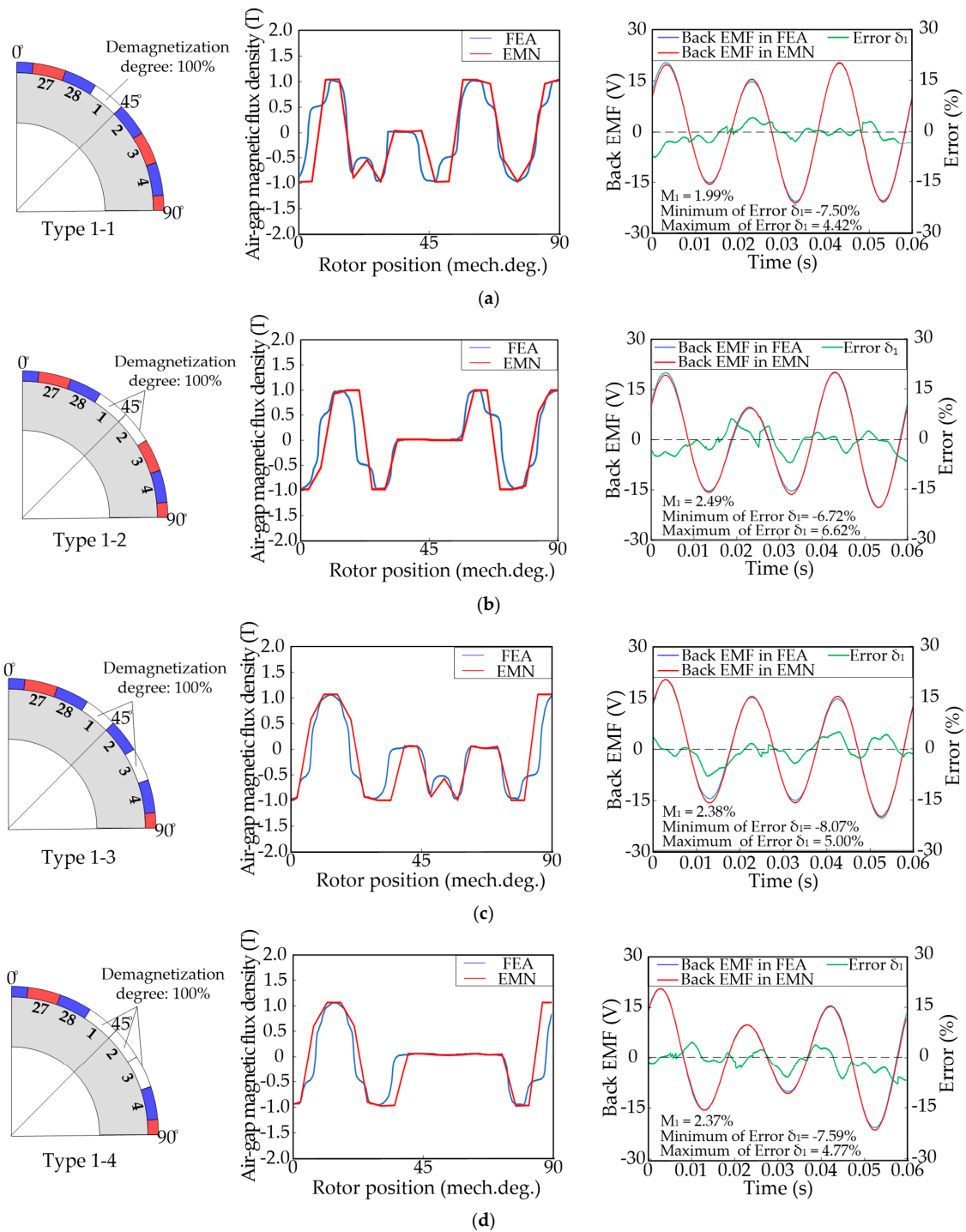


**Figure 12.** The result comparison of demagnetization Group 1, (a) demagnetization type 1-1, (b) demagnetization type 1-2, (c) demagnetization type 1-3, (d) demagnetization type 1-4.

In addition, for demagnetization Group 2, the result comparison between the FEA and the proposed EMN model in the condition of the constant rated rotating speed of the rotor is shown in Figure 13. The air-gap flux density waveforms obtained by the proposed EMN model also well matches with the FEA results. And the absolute value of the transient error  $\delta_1$  is less than 8.3%, and  $M_1$  is between 2.68% and 3.16%. From above comparison, the proposed EMN model is highly identical to the FEA, thus evidencing its validity for accurately analyzing the demagnetization characteristics of the six-phase surface-mounted FMPMM.

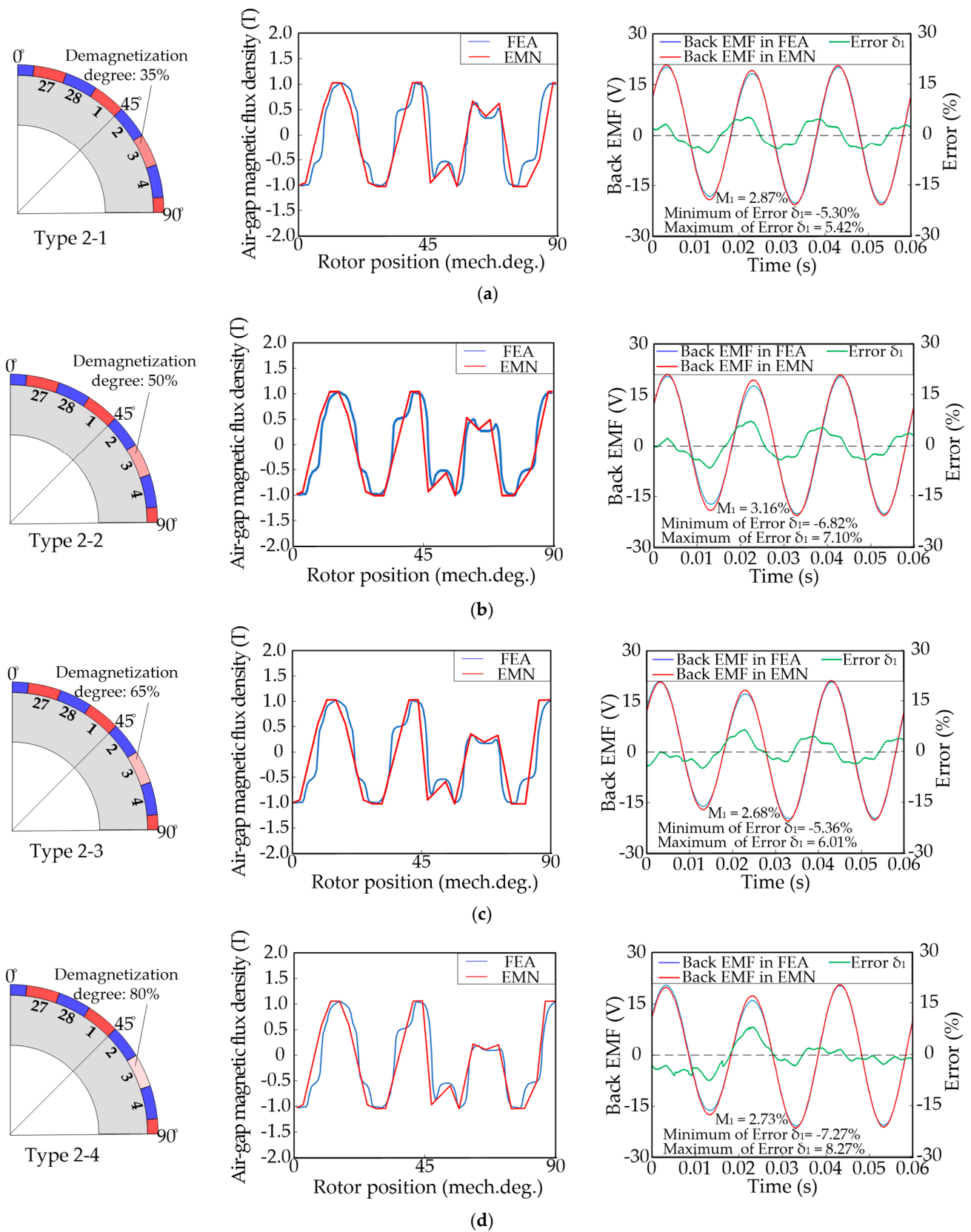


**Figure 13.** The result comparison of demagnetization Group 2, (a) demagnetization type 2-1, (b) demagnetization type 2-2, (c) demagnetization type 2-3, (d) demagnetization type 2-4.

Furthermore, the calculation time of model is also concerned. The calculation time of the FEA and the proposed EMN model is shown in Table 9. In this paper, the number of grids in the FEA is 10,322, and its calculation time is 447 s. However, the number of grids in the proposed EMN model is 352, and the calculation time is only 102 s. By comparison, it is confirmed that the proposed EMN model needs less calculation time than the FEA under the condition of ensuring proper accuracy.

**Table 9.** Calculation comparison between the proposed EMN model and the FEA.

Methods	Comparative Terms	
	The Number of Grids	Calculation Time
FEA	10,322	447 s
Proposed EMN	352	102 s

## 5. Experimental Verification

In order to further verify the validity of the proposed EMN model, a prototype is fabricated, and the main parameters of prototype are the same as Table 1. In order to achieve the superiority in the aspect of the economy under the condition of meeting the requirements of machine performance, the material of the iron core of the prototype is 35CS250 silicon steel, and the type of the material of the permanent magnet is N38SH. These two materials are common in the market and low in price. As shown in Figure 14, the PMs of the prototype are closely attached to the surface of the rotor iron core. In the manufacturing process, the three PMs (PM1, PM7, PM8) of the prototype are removed and replaced by stainless steel blocks with the same shape as the PMs to imitate demagnetization. The testing platform based on the prototype is shown in Figure 15, in which the servo motor controlled by dSPACE1103 drives the prototype operating in diverse speeds [35,36], and the no-load back EMF of the prototype can be recorded by Oscilloscope.

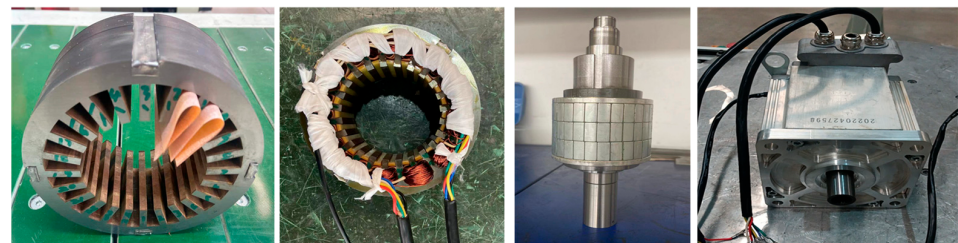


**Figure 14.** Prototype manufacturing and assembly.



**Figure 15.** Testing platform of the prototype.

As shown in Figure 16, the no-load back-EMF waveforms obtained by the proposed EMN model, the FEA, and the experimental testing at the rated speed 214 r/min are compared. In order to reflect the no-load back EMF error more intuitively, the transient error of the no-load back EMF between the EMN and the prototype is  $\delta_2$ , and the MAE of the transient error  $\delta_2$  is  $M_2$ , which is expressed as

$$\delta_2(t) = \frac{v_{EMN}(t) - v_{pro}(t)}{V_{peak}} \times 100\% \quad (13)$$

$$M_2 = \frac{\int_{t_1}^{t_2} |\delta_2(t)| dt}{t_2 - t_1} \quad (14)$$

where  $v_{pro}(t)$  is the no-load back EMF obtained by the experimental testing at time  $t$ .

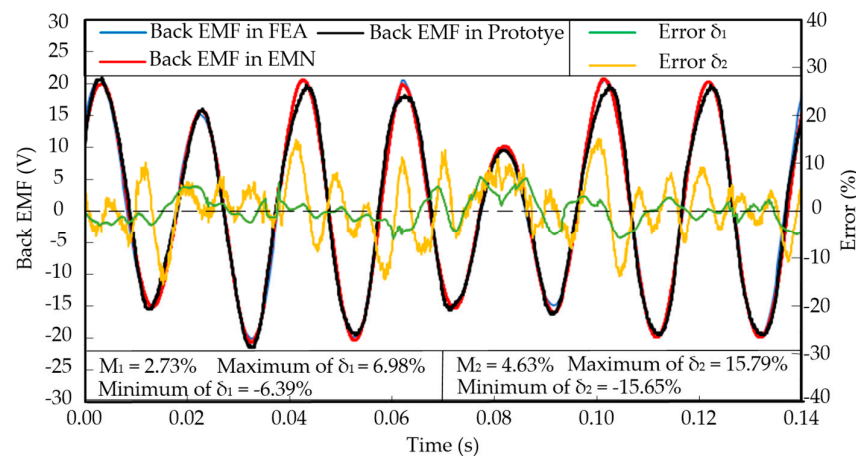


**Figure 16.** Comparison of no-load back-EMF waveforms at rated speed 214 r/min.

In accordance with the above conclusion, the no-load back-EMF waveforms obtained by the proposed EMN model almost match the FEA results. And the absolute value of the transient error  $\delta_1$  between them is less than 7%, and the  $M_1$  is 2.73%. Moreover, the experimental no-load back-EMF waveforms also agree with the results obtained by the proposed EMN model and the FEA. That is, the absolute value of the transient error  $\delta_2$  between the proposed EMN model and experimental testing is not larger than 16%, and  $M_2$  is about 4.63%, which is acceptable.

Furthermore, a series of no-load back-EMF waveforms at different speeds are experimentally measured and compared with the proposed EMN model and the FEA results. Figure 17a,b show the transient error  $\delta_1$  and  $\delta_2$ , respectively. It can be seen from Figure 17a that the absolute value of the transient  $\delta_1$  at different speeds is always less than 12.5%, and  $M_1$  is less than 4%. And it can be found that from 90 r/min to 300 r/min,  $M_1$  basically fluctuates between 3% and 3.5%, which means there is a good consistence in the no-load back EMF waveform between the proposed EMN model and the FEA in a wide range of speeds. Similarly, it can be seen from Figure 17b that the absolute value of the transient error  $\delta_2$  at speeds below 240 r/min is about less than 15%, and  $M_2$  is less than 5.5%. Compared with the transient error  $\delta_1$ ,  $\delta_2$  is a little larger, and it can be explained that the end effects are not considered in the proposed EMN model and FEA, thus causing the no-load back EMF discount in the prototype testing as shown in Figure 16. Anyway, the results show that the proposed EMN model is an effective method for evaluating the demagnetization characteristics of the analyzed six-phase surface-mounted FMPMM in a wide range of speeds.

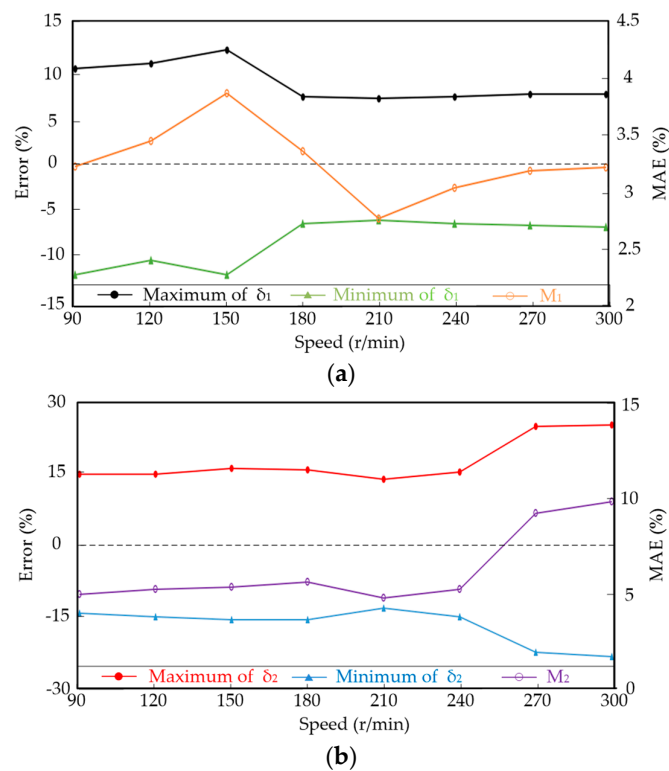


**Figure 17.** Comparison of no-load back EMF error at different speeds, (a) the transient error  $\delta_1$  and  $M_1$ , (b) the transient error  $\delta_2$  and  $M_2$ .

## 6. Conclusions

In this paper, the six-phase surface-mounted FMPMM demagnetization model based on the EMN method was established and evaluated. In order to realize a rapid EMN modeling and accurate result analysis of the six-phase surface-mounted FMPMM under different demagnetization types, the coercivity variable and the curve-fitting method were introduced. Also, the air-gap flux density and the no-load back EMF waveforms were obtained by the proposed EMN model, the FEA, and the prototype experiments, respectively. By comparison, it was shown that the results obtained by the proposed EMN model are consistent with the FEA and experimental testing. Also, the selected materials met the economy and the performance of the machine operation. At the same time, the proposed EMN model required a shorter calculation time than the FEA. In consequence, the proposed EMN model not only enriched the method for modeling FMPMM demagnetization mode, but also provided a reference for a demagnetization diagnosis of the machine.

**Author Contributions:** Data curation, Y.Z. and H.W.; Writing—original draft, Y.T.; Writing—review & editing, B.Y.; Supervision, X.L.; Project administration, X.L. All authors have read and agreed to the published version of the manuscript.

**Funding:** This research was funded in part by the Regional Innovation and Development Joint Fund of National Natural Science Foundation of China under Grant U22A20218; in part by the Shandong Provincial Natural Science Foundation of China under Grant ZR2021YQ33; and in part by the Natural Science Foundation of Shandong Province under Grant ZR2022QE247.

**Data Availability Statement:** No new data were created or analyzed in this study. Data sharing is not applicable to this article.

**Conflicts of Interest:** The authors declare no conflict of interest.

## References

1. Liu, J.; Li, X.; Yan, B.; Hua, W.; Wang, X. Electromagnetic Performance Analysis of a Field-Modulated Permanent Magnet Motor Using Improved Hybrid Subdomain Method. *IEEE Trans. Energy Convers.* **2023**. Early Access. [[CrossRef](#)]
2. Li, X.; Wei, Z.; Zhao, Y.; Wang, X.; Hua, W. Design and Analysis of Surface-Mounted Permanent-Magnet Field-modulation Machine for Achieving High Power Factor. *IEEE Trans. Ind. Electron.* **2023**. Early Access. [[CrossRef](#)]
3. Li, X.; Liu, S.; Wang, Q.; Yan, B.; Huang, Z.; Wang, K. Performance Investigation and Experimental Testing of a Stator-PM-Excitation Axial-Flux Magnetic Gear. *IEEE Trans. Transport. Electrification.* **2023**, *9*, 2593–2605. [[CrossRef](#)]
4. Li, X.; Chau, K.; Cheng, M.; Kim, B.; Lorenz, R. Performance Analysis of a Flux-Concentrating Field-Modulated Permanent-Magnet Machine for Direct-Drive Applications. *IEEE Trans. Magn.* **2015**, *51*, 8104911. [[CrossRef](#)]
5. Jing, L.; Liu, W.; Tang, W.; Qu, R. Design and Optimization of Coaxial Magnetic Gear with Double-Layer PMs and Spoke Structure for Tidal Power Generation. *IEEE/ASME Trans. Mechatron.* **2023**. Early Access. [[CrossRef](#)]
6. Jing, L.; Tang, W.; Wang, T.; Ben, T.; Qu, R. Performance Analysis of Magnetically Geared Permanent Magnet Brushless Motor for Hybrid Electric Vehicles. *IEEE Trans. Transp. Electrification.* **2022**, *8*, 2874–2883. [[CrossRef](#)]
7. Zhao, H.; Liu, C.; Dong, Z.; Huang, R.; Li, X. Design and Optimization of a Magnetic-Geared Direct-Drive Machine with V-Shaped Permanent Magnets for Ship Propulsion. *IEEE Trans. Transport. Electrification.* **2022**, *8*, 1619–1633. [[CrossRef](#)]
8. Jing, L.; Wang, T.; Tang, W.; Liu, W.; Qu, R. Characteristic Analysis of the Magnetic Variable Speed Diesel-Electric Hybrid Motor with Auxiliary Teeth for Ship Propulsion. *IEEE/ASME Trans. Mechatron.* **2023**. Early Access. [[CrossRef](#)]
9. Zhou, P.; Lin, D.; Xiao, Y.; Lambert, N.; Rahman, M. Temperature-Dependent Demagnetization Model of Permanent Magnets for Finite Element Analysis. *IEEE Trans. Magn.* **2012**, *48*, 1031–1034. [[CrossRef](#)]
10. Woo, D.; Jeong, B. Irreversible Demagnetization of Permanent Magnet in a Surface-Mounted Permanent Magnet Motor with Overhang Structure. *IEEE Trans. Magn.* **2016**, *52*, 8102606. [[CrossRef](#)]
11. Fernández, D.; Martínez, M.; Reigosa, D.; Guerrero, J.; Alvarez, C.; Briz, F. Permanent Magnets Aging in Variable Flux Permanent Magnet Synchronous Machines. *IEEE Trans. Ind. Appl.* **2020**, *56*, 2462–2471. [[CrossRef](#)]
12. Kim, H.; Park, J.; Hur, J. Comparison Analysis of Demagnetization and Torque Ripple in Accordance with Freewheeling Current in PM BLDC Motor. *IEEE Trans. Magn.* **2015**, *51*, 8108204. [[CrossRef](#)]
13. Chen, H.; Qu, R.; Li, J.; Li, D. Demagnetization Performance of a 7 MW Interior Permanent Magnet Wind Generator with Fractional-Slot Concentrated Windings. *IEEE Trans. Magn.* **2015**, *51*, 8205804. [[CrossRef](#)]
14. Kang, D. Analysis of Vibration and Performance Considering Demagnetization Phenomenon of the Interior Permanent Magnet Motor. *IEEE Trans. Magn.* **2017**, *53*, 8210807. [[CrossRef](#)]
15. Kim, K.; Kim, K.; Kim, H.; Lee, J. Demagnetization Analysis of Permanent Magnets According to Rotor Types of Interior Permanent Magnet Synchronous Motor. *IEEE Trans. Magn.* **2009**, *45*, 2799–2802. [[CrossRef](#)]
16. Guo, L.; Wang, K.; Wang, T. Open-Circuit Fault Diagnosis of Three-Phase Permanent Magnet Machine Utilizing Normalized Flux-Producing Current. *IEEE Trans. Ind. Electron.* **2023**. Early Access. [[CrossRef](#)]
17. Lin, D.; Zhou, P.; Bracken, E. Generalized Algorithm to Deal with Temperature-Dependent Demagnetization Curves of Permanent Magnets for FEA. *IEEE Trans. Magn.* **2021**, *57*, 7402706. [[CrossRef](#)]
18. Fu, W.; Ho, S. Dynamic Demagnetization Computation of Permanent Magnet Motors Using Finite Element Method with Normal Magnetization Curves. *IEEE Trans. Appl. Supercond.* **2010**, *20*, 851–855. [[CrossRef](#)]
19. Zhang, J.; Jiang, Y.; Zhao, J.; Hua, W. An Improved Brushless Doubly Fed Generator with Interior PM Rotor for Wind Power Applications. *IEEE Trans. Magn.* **2019**, *55*, 8105506. [[CrossRef](#)]
20. Bisschop, J.; Abdallah, A.; Sergeant, P.; Dupré, L. Identification of Demagnetization Faults in Axial Flux Permanent Magnet Synchronous Machines Using an Inverse Problem Coupled with an Analytical Model. *IEEE Trans. Magn.* **2014**, *50*, 8104804. [[CrossRef](#)]
21. Verkroost, L.; De Bisschop, J.; Vansompel, H.; Belie, F.; Sergeant, P. Active Demagnetization Fault Compensation for Axial Flux Permanent-Magnet Synchronous Machines Using an Analytical Inverse Model. *IEEE Trans. Energy Convers.* **2020**, *35*, 591–599. [[CrossRef](#)]
22. Bisschop, J.; Vansompel, H.; Sergeant, P.; Dupre, L. Demagnetization Fault Detection in Axial Flux PM Machines by Using Sensing Coils and an Analytical Model. *IEEE Trans. Magn.* **2017**, *53*, 8203404. [[CrossRef](#)]
23. Gong, C.; Deng, F. Demagnetization Analysis of a Split-Tooth Concentrated-Winding Vernier Machine using Halbach-array-based Ferrite Magnets. In Proceedings of the 2021 IEEE International Electric Machines & Drives Conference (IEMDC), Hartford, CT, USA, 17–20 May 2021. [[CrossRef](#)]
24. Li, L.; Fu, W.; Ho, S.; Niu, S.; Li, Y. A Quantitative Comparison Study of Power-Electronic-Driven Flux-Modulated Machines Using Magnetic Field and Thermal Field Co-Simulation. *IEEE Trans. Ind. Electron.* **2015**, *62*, 6076–6084. [[CrossRef](#)]
25. Li, X.; Chau, K.; Wang, Y. Modeling of a Field-Modulated Permanent-Magnet Machine. *Energies* **2016**, *9*, 1078. [[CrossRef](#)]
26. Tong, C.; Song, Z.; Bai, J.; Liu, J.; Zheng, P. Analytical Investigation of the Magnetic-Field Distribution in an Axial Magnetic-Field-Modulated Brushless Double-Rotor Machine. *Energies* **2016**, *9*, 589. [[CrossRef](#)]
27. Oner, Y.; Zhu, Z.; Wu, L.; Ge, X.; Zhan, H.; Chen, J. Analytical On-Load Subdomain Field Model of Permanent-Magnet Vernier Machines. *IEEE Trans. Ind. Electron.* **2016**, *63*, 4105–4117. [[CrossRef](#)]
28. Cao, D.; Zhao, W.; Ji, J.; Ding, L.; Zheng, J. A Generalized Equivalent Magnetic Network Modeling Method for Vehicular Dual-Permanent-Magnet Vernier Machines. *IEEE Trans. Energy Convers.* **2019**, *34*, 1950–1962. [[CrossRef](#)]

29. Li, X.; Lu, K.; Zhao, Y.; Chen, D.; Yi, P.; Hua, W. Incorporating harmonic-analysis-based loss minimization into MPTC for efficiency improvement of FCFMPM motor. *IEEE Trans. Ind. Electron.* **2023**, *70*, 6540–6550. [[CrossRef](#)]
30. Ostovic, V. A simplified approach to magnetic equivalent-circuit modeling of induction machines. *IEEE Trans. Ind. Appl.* **1988**, *24*, 308–316. [[CrossRef](#)]
31. Cao, D.; Zhao, W.; Liu, T.; Wang, Y. Magneto-Electric Coupling Network Model for Reduction of PM Eddy Current Loss in Flux-Switching Permanent Magnet Machine. *IEEE Trans. Ind. Electron.* **2022**, *69*, 1189–1199. [[CrossRef](#)]
32. Fleming, F.; Edrington, C. Real-Time Emulation of Switched Reluctance Machines via Magnetic Equivalent Circuits. *IEEE Trans. Ind. Electron.* **2016**, *63*, 3366–3376. [[CrossRef](#)]
33. Ghods, M.; Gorginpour, H.; Bazrafshan, M.; Toulabi, M. Equivalent Magnetic Network Modeling of Dual-Winding Outer-Rotor Vernier Permanent Magnet Machine Considering Pentagonal Meshing in the Air-Gap. *IEEE Trans. Ind. Electron.* **2022**, *69*, 12587–12599. [[CrossRef](#)]
34. Cao, D.; Zhao, W.; Ji, J.; Wang, Y. Parametric Equivalent Magnetic Network Modeling Approach for Multiobjective Optimization of PM Machine. *IEEE Trans. Ind. Electron.* **2021**, *68*, 6619–6629. [[CrossRef](#)]
35. Li, X.; Xue, Z.; Zhang, L.; Hua, W. A Low-Complexity Three-Vector-Based Model Predictive Torque Control for SPMSM. *IEEE Trans. Power Electron.* **2021**, *36*, 13002–13012. [[CrossRef](#)]
36. Li, X.; Xue, Z.; Yan, X.; Zhang, L.; Ma, W.; Hua, W. Low-Complexity Multivector-Based Model Predictive Torque Control for PMSM With Voltage Preselection. *IEEE Trans. Power Electron.* **2021**, *36*, 11726–11738. [[CrossRef](#)]

**Disclaimer/Publisher’s Note:** The statements, opinions and data contained in all publications are solely those of the individual author(s) and contributor(s) and not of MDPI and/or the editor(s). MDPI and/or the editor(s) disclaim responsibility for any injury to people or property resulting from any ideas, methods, instructions or products referred to in the content.